VIRTUAL AND PHYSICAL PROTOTYPING
2025, VOL. 20, NO. 1, e2474537 (14 pages)
https://doi.org/10.1080/17452759.2025.2474537

Taylor & Francis
Taylor & Francis Group

4D printing of multiscale filler–reinforced thermoplastic polyurethane nanocomposites with electro-activated shape memory properties

Meixin Zhou[a], Yujia Tian [a], Mui Ling Sharon Nai[b], H. Jerry Qi[c] and Kun Zhou [a]

[a]Singapore Centre for 3D Printing, School of Mechanical and Aerospace Engineering, Nanyang Technological University, Singapore, Singapore; [b]Singapore Institute of Manufacturing Technology, Agency for Science, Technology and Research, Singapore, Singapore; [c]School of Mechanical Engineering, Georgia Institute of Technology, Atlanta, GA, USA

ABSTRACT

Four-dimensional printing of shape memory materials has been developed to dynamically control the shapes of printed structures for applications such as self-deployable structures, actuators, and sensors. Herein, a novel electro-activated shape memory nanocomposite material for the selective laser sintering (SLS) process is developed. The nanocomposite powder incorporates a new type of multiscale hybrid filler, consisting of carbon fibres and carbon nanotubes (CNTs), with CNT-coated thermoplastic polyurethane nanocomposite powders. The shape recovery process of the nanocomposite with a 20 wt% hybrid-filler addition is almost four times faster when triggered by electric currents than that triggered by the direct heating method and exhibits a higher shape recovery ratio. A remotely and selectively controlled smart component is fabricated to demonstrate the potential applications of the novel nanocomposites. This work provides a promising solution to achieve function–structure integration through SLS for future high-tech applications.

ARTICLE HISTORY
Received 19 December 2024
Accepted 26 February 2025

KEYWORDS
4D printing; selective laser sintering; shape memory polymer composite

1. Introduction

Stimuli-responsive materials have the capability of responding to an external stimulus, such as heat [1–3], moisture, light, and pH value changes [4], and have attracted significant research interests. Among these materials, shape memory polymers (SMPs) have been one of the most studied candidates for applications including self-deployable structures [5,6], actuators [7–10], and sensors [11]. Electro-activated SMPs show great potential in broadening the applications of SMPs because of their capability of easy operation and remote control. Electro-activated shape memory polymer composites (SMPCs) have been developed by introducing conductive fillers such as metallic particles [12–16], carbon nanoparticles [17–20], hybrid conductive fillers [21–23], and conductive polymers [24,25] into the polymer matrix to establish an electrically conductive network for shape recovery by the Joule heating effect. However, the potential of the developed electro-activated SMPs is limited by the simplicity of structures fabricated by traditional manufacturing methods. Moreover, realising electro-activated shape recovery often necessitates a high filler content, thereby imposing further challenges in employing traditional manufacturing technologies.

In recent years, four-dimensional (4D) printing has shown tremendous potential for fabricating programmable structures using electro-activated SMPs *via* polymer three-dimensional (3D) printing techniques. 4D printing has gained significant attention in defence, aerospace, biomedical engineering [26–28], *etc*. So far, conductive materials like silver nanowires [29], carbon fibres (CFs) [30], and carbon nanotubes (CNTs) [31] have been incorporated *via* the fused deposition modelling 3D printing technique to control the shape transformation through electricity. Additionally, co-extrusion [32] and digital light processing techniques [33] have been applied to fabricate electro-activated SMPCs with improved heating rates and functional properties. However, the research on 4D printing of electro-activated SMPCs is insufficient, and few studies have employed the selective laser sintering (SLS) 3D printing technique, which is one of the laser powder bed fusion techniques according to ISO 52900. Compared with

CONTACT Kun Zhou kzhou@ntu.edu.sg Singapore Centre for 3D Printing, School of Mechanical and Aerospace Engineering, Nanyang Technological University, Singapore 639798, Singapore

Supplemental data for this article can be accessed online at https://doi.org/10.1080/17452759.2025.2474537.

other polymer 3D printing techniques, SLS has the advantages of high fabrication speed, high design freedom due to no need for supporting materials, and being free of shear stress during the fabrication process. The last advantage has been proved to facilitate the establishment of an electrically conductive network [34]. By leveraging the unique capabilities of SLS, researchers have endeavoured to developing conductive materials [34–39]. While many of these studies have focused on applications in piezoresistive sensors [34,40–44], the potential for SLS-printed electro-activated shape memory materials in smart components remains largely unexplored.

This work develops a novel electro-activated shape memory nanocomposite fabricated *via* SLS and presents its electro-activated shape memory behaviours and underlying mechanism. A type of multiscale conductive hybrid filler (HF) that contains CFs and CNTs was first developed to facilitate the establishment of a conductive network at a low filler content. The fillers were then added into a CNT-coated thermoplastic polyurethane (TPU) nanocomposite powder. The prepared powder was systematically evaluated for the SLS process, and the process parameters were optimised. The SLS-printed nanocomposite exhibited a much faster shape recovery when triggered by Joule heating than by the direct heating method, illustrating its high efficiency in actuating shape transformation. A remotely controlled smart component, whose shape transformation can be selectively triggered, was fabricated to demonstrate its advantages of fast response and easy operation. This work provides fundamental insights into developing electro-activated SMP nanocomposite powders that are compatible with the SLS process, paving the way for employing 4D printing of electro-activated SMPCs in various applications.

2. Material and method

2.1. Materials

TPU powder with a density of 1.2 g/cm^3, sourced from Lehmann & Voss Corp., Germany, was used in this study. Hydroxyl-functionalised multi-walled carbon nanotubes, annotated as CNT–OH, were selected as the primary nanofiller for the nanocomposite development. They were purchased from TimestubTM Ltd., China, and have an outer diameter of 5–15 nm and a length of 10–30 µm. CFs, purchased from ZoltekTM Inc., USA, were plasma treated by Tech-in Materials Ltd., China to increase the hydrophilicity of their surface before they were employed as the secondary filler for the nanocomposite development. They have a diameter of 7.2 µm and an average length of 100 µm. Hexamethylene diisocyanate (HDI), purchased from Macklin Biochemical Ltd., China, was used as received. Dibutyltin dilaurate (DBTDL), *N*, *N*–Dimethylformamide (DMF), and acetone, all purchased from Sigma-Aldrich Ltd., USA, were used as received.

2.2. Development of the hybrid filler and nanocomposite powders

To achieve desirable electro-activated shape memory performance with a low filler content, a conductive hybrid filler was developed. The hybrid filler is multiscale and was prepared by grafting CNT–OH onto plasma-treated CFs, with HDI linking the two carbon-based fillers (Figure 1a). HDI also aids in facilitating the dispersion of the hybrid filler into the polymer matrix, thereby enhancing the fibre–matrix interface. First, the plasma-treated CFs and HDI with a weight ratio of 1:2 were mixed with the DMF solution in a four-neck flask, and the mixture was then heated to 80 °C in an oil bath and magnetically stirred at 1400 rpm under the nitrogen atmosphere. The catalyst DBTDL was then added dropwise into the mixture. After being heated and stirred for 3 h, the mixture was cooled down to room temperature, filtered to remove the liquid, washed with acetone, and dried in a vacuum oven at 80 °C to obtain HDI-grafted CFs. HDI-grafted CFs and CNT-OH, with a weight ratio of 99:1, were added to the DMF solution. This ratio was selected so that the weight ratio of CNT–OH in the prepared TPU nanocomposites is 1%, a value determined based on our previous work [39] to achieve a good balance between the desired electrical conductivity and the processability of the SLS powders. The mixture was then heated to 80°C and stirred at 1400 rpm for 3 h under a nitrogen atmosphere. Meanwhile, DBTDL was also added dropwise into the mixture. The mixture was then filtered and dried to obtain the hybrid filler (CF–CNT) with CNT–OH coating on the surface of HDI-grafted CFs.

The hybrid filler–reinforced nanocomposite powders were prepared in two steps (Figure 1b). First, a TPU-based nanocomposite powder with 1.0 wt% CNT–OH was prepared based on a method elaborated in our previous study [39]. The 1.0 wt% CNT–OH/TPU nanocomposite powder was then mixed with the developed hybrid filler by a tumbler mixer (Inversina 2L, Bioengineering AG, Switzerland) at a rotation speed of 70 rpm for 3 h. The nanocomposite powders with different hybrid-filler contents (10, 20, and 30 wt%) were prepared. In this study, the control group without the addition of the CF–CNT hybrid filler was annotated as HF0, and the nanocomposite powders with different HF contents of

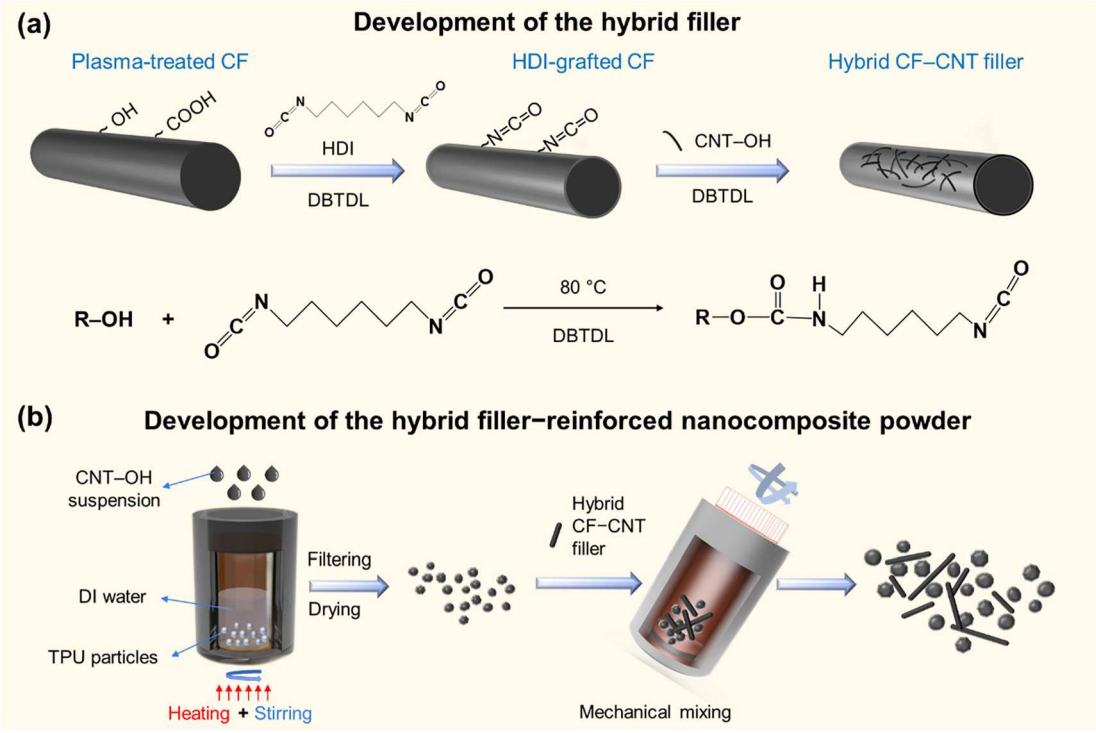

Figure 1. Development process of multiscale hybrid filler–reinforced TPU nanocomposite powders for the SLS process: (a) development of the hybrid filler; (b) development of the hybrid filler–reinforced nanocomposite powder.

10, 20, and 30 wt% were prepared and labelled as HF10, HF20, and HF30, respectively.

2.3. Specimen fabrication

A desktop SLS machine (Snowwhite2, Sharebot S.R.L., Italy) was used for specimen fabrication. The powder bed temperature was set at 100 °C. The optimisation of process parameters consisted of two steps. Specimens were first printed under different E_{vol} (0.3, 0.5, and 0.7 J/mm^3) by tuning the laser power p (7.2, 12.0, and 16.8 W, respectively) and fixing the scan speed s at 2000 mm/s, the hatching distance h at 0.1 mm, and the layer thickness L at 0.12 mm according to

$$E_{vol} = \frac{p}{shL}. \quad (1)$$

The scan speed was considered as another critical process parameter which should be optimised to enhance the sintering degree of nanocomposite powder particles. Under the optimal E_{vol} value, different scan speeds (500, 1000, 1500, and 2000 mm/s) and laser power (4.2, 8.4, 12.6, and 16.8 W, respectively) were used with a hatching distance of 0.1 mm and a layer thickness of 0.12 mm to find the optimised parameter set. The HF10, HF20, and HF30 nanocomposite powders as well as the designed structures were all printed under the optimised combination of process parameters.

2.4. Characterisation

A field emission scanning electron microscope (FESEM, JEOL 7600, JEOL Corp., Japan) under an accelerating voltage of 5 kV was used to observe the morphology of the developed fillers. An X-ray photoelectron spectroscope (XPS, AXIS Supra, Kratos Analytical Ltd., UK) was employed to explore the chemical composition of the surface of the developed hybrid filler.

The powder characteristics including the particle size and particle size distribution, particle morphology, and powder flowability were characterised following the methods illustrated in our previous work [45]. The heating and cooling behaviours as well as decomposition temperature of the powder were characterised by a differential scanning calorimeter (DSC, Q200, TA Instruments Ltd., USA) and a thermogravimetric analyser (TGA, Q500, TA Instruments Ltd., USA), respectively, following established and widely accepted protocols [39]. The coalescence behaviour of the powder was evaluated by measuring the melt viscosity through a temperature sweep performed on a rotational rheometer (Discovery

HR, TA instruments Ltd., USA) by decreasing the temperature from 200 °C to 80 °C with a controlled rate of 5 °C/min under a shear rate of 0.05 s^{-1} [39].

The tensile properties of the SLS-printed ASTM D638 Type-V specimens were evaluated using a universal tester (AGX 10 KN, Shimadzu Corp., Japan) at 23 °C with a crosshead speed of 50 mm/min. To ensure reproducibility, a minimum of three samples were tested, and their average values were recorded.

The electrical resistance of the specimens ($20 \times 10 \times 0.6$ mm^3) was measured by a source metre (2450, Keithley Instruments Inc., USA) at room temperature under a fixed voltage of 200 V [39]. The volume electrical conductivity σ was calculated according to

$$\sigma = \frac{d}{RS}, \tag{2}$$

where d, R and S are the gauge length, electrical resistance, and cross-sectional area of the specimen, respectively. The electro-heating behaviours of the specimens ($20 \times 10 \times 0.6$ mm^3), affixed with two strips of conductive copper tapes for connection to the source metre, were investigated. Different voltages (50, 100, 150, and 200 V) were applied, and the changes in the surface temperature of each sample were recorded using an infrared camera (PI 450i, Optris GmbH, Germany) for 3 min.

The shape memory behaviours of the prepared nanocomposites were investigated using specimens with dimensions of $40 \times 10 \times 0.6$ mm^3. The specimens were bent 180° in an oven at 100 °C, and the temporary shape was fixed after cooling the samples to room temperature and releasing the bending force. Conductive wires were attached to the samples using conductive silver glue and copper tapes. The shape recovery process was recorded using the infrared camera once the samples were connected to the source metre through the conductive wires. The direct heating–activated shape memory behaviour was observed by placing the specimens on a hot plate (BYA, Sichuan Bangyuan Technology Ltd., China) with its surface temperature at 120 °C and recording the changes in the shape *via* the infrared camera.

The shape recovery ratio R_r is a critical parameter for evaluating the shape memory behaviours of materials as it indicates the ability of a material to return to its original shape after deformation. A high shape recovery ratio is favoured in practical applications. The shape recovery ratio was calculated based on

$$R_r = \frac{\theta_{deformed} - \theta_{unrecovered}}{\theta_{deformed}} \times 100\%, \tag{3}$$

where $\theta_{deformed}$ and $\theta_{unrecovered}$ are the deformed angle after the temporary fixation and the residual deformed angle after the stimulation, respectively. Their values were obtained by the software Image J. In this study, shape memory properties were quantitatively compared using the indicators of the shape recovery ratio R_{r_25} and R_{r_600} when the shape recovery time reached 25 s and 600 s, respectively.

3. Results and discussion

3.1. Development and evaluation of the nanocomposite powder

The multiscale hybrid filler was developed by grafting CNT–OH on the surface of plasma-treated CFs with the assistance of HDI (Figure 1a). The plasma-treated CFs exhibited some small surface grooves that were conducive to the absorption of HDI [46] and some small particles attached (Figure 2a). Then, HDI was grafted on the surface of the plasma-treated CFs through the additive reaction between the cyanate groups (–N=C=O) and the oxygen-containing groups (–OH/–COOH) (Figure 2b). Next, the remaining cyanate groups of the HDI-grafted CFs reacted with the added CNT–OH, yielding hybrid CF–CNT fillers. The surface of the hybrid filler became rough, and CNT–OH was uniformly distributed on the surface as observed from the FESEM image with a higher magnification (Figure 2c).

To further confirm the microstructure of the developed hybrid filler, the chemical bonds of CNT–OH, plasma-treated CFs, HDI-grafted CFs, and hybrid CF–CNT fillers were characterised. The peaks in the O 1s spectra suggest that both CNT–OH and plasma-treated CFs might contain hydroxyl groups (Figures S1a and S1b), which were the active sites reacting with the bridge material HDI [47]. The peaks at ~284.6 eV and 285.2 eV in the C 1s spectra correspond to the C=C and C–C bonds, respectively (Figure 2d), which are commonly reported in carbon-based fillers [48–51]. The cyanate groups (–N=C=O) from HDI were confirmed to be bonded with oxygen-containing groups from the plasma-treated CFs and CNT–OH as the peak located at ~288.5 eV in the C 1s spectra was attributed to the existence of the HN–C=O bond [47]. A higher –COO content was found in the hybrid CF–CNT fillers than in the HDI-grafted CFs, which could be attributed to the reactions between CNT–OH and the HDI-grafted CFs. Additionally, as shown in the N 1s spectra, the HN–C=O bond content increased significantly in the hybrid CF–CNT fillers compared to that of the HDI-grafted CFs (Figure S1c) and hybrid CF–CNT fillers (Figure S1d), suggesting that the HN–C=O bond was formed between HDI and CNT–OH. These results confirm that

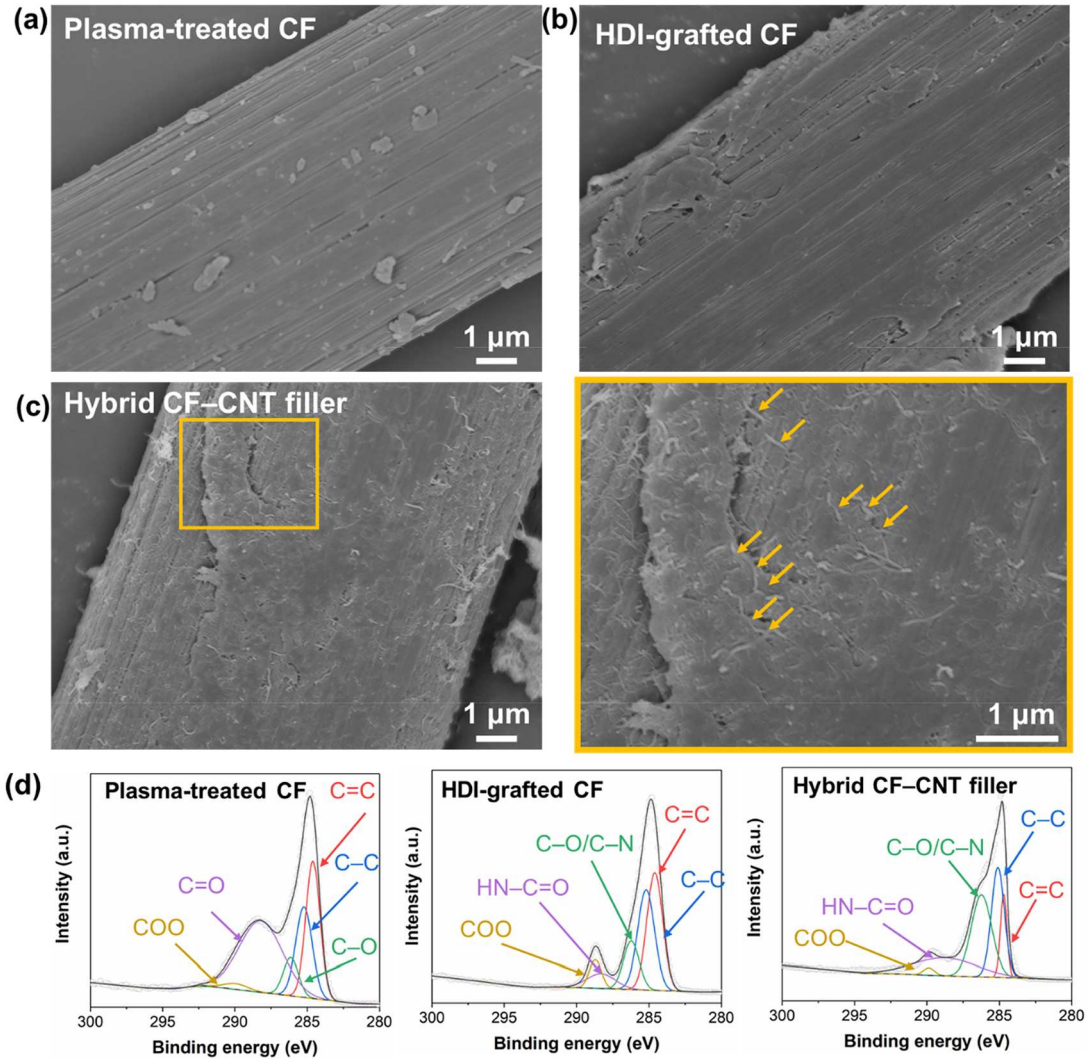

Figure 2. Characterisation of the developed fillers: morphology of (a) a plasma–treated CF, (b) an HDI-grafted CF, and (c) a CF–CNT hybrid filler; (d) XPS C 1s spectra of the developed fillers.

the hybrid CF–CNT filler was successfully developed by grafting CNT–OH to the plasma-treated CFs with HDI connecting the two carbon-based fillers.

The functional nanocomposite powder for the SLS process was then prepared by mechanically mixing the hybrid CF–CNT filler with CNT–OH-coated TPU powders (Figure 1b). The processability of the HF0, HF10, HF20, and HF30 nanocomposite powders in the SLS process was systematically evaluated based on powder, thermal, and rheological properties.

An ideal powder candidate for the SLS process should possess a spherical particle shape (sphericity closer to 1), an appropriate particle size and size distribution, a high packing density, as well as a proper Hausner ratio (less than 1.25 [52]) and avalanche angle (within the range of 40–60° [53]). Spherical particles could facilitate the powder flow, while small particles (<45 μm [54]) prone to impede the powder flow. A higher packing efficiency ensures a denser power bed, which leads to increased part density.

The prepared nanocomposite powder was composed of CNT–OH-coated TPU particles and the rod-like hybrid filler (~100 μm in length) (Figure 3a and Figure S2). The CNT–OH-coated TPU particles maintained the irregular shape of the uncoated TPU particles (~100 μm in volume-weighted mean particle size $D_{[4,3]}$). The irregularly shaped particles and the existence of the rod-like hybrid CF–CNT fillers could result in a coarse powder bed indicated by high surface roughness and the presence of localised holes or bumps [55]. The $D_{[4,3]}$ value of the HF20 nanocomposite powder was 86.3 μm (Table S1), aligning with the recommended average particle size for the SLS process [54]. Additionally, the introduction of the hybrid CF–CNT fillers increased the proportion of smaller-sized particles, thereby broadening the particle size distribution (Figure S2).

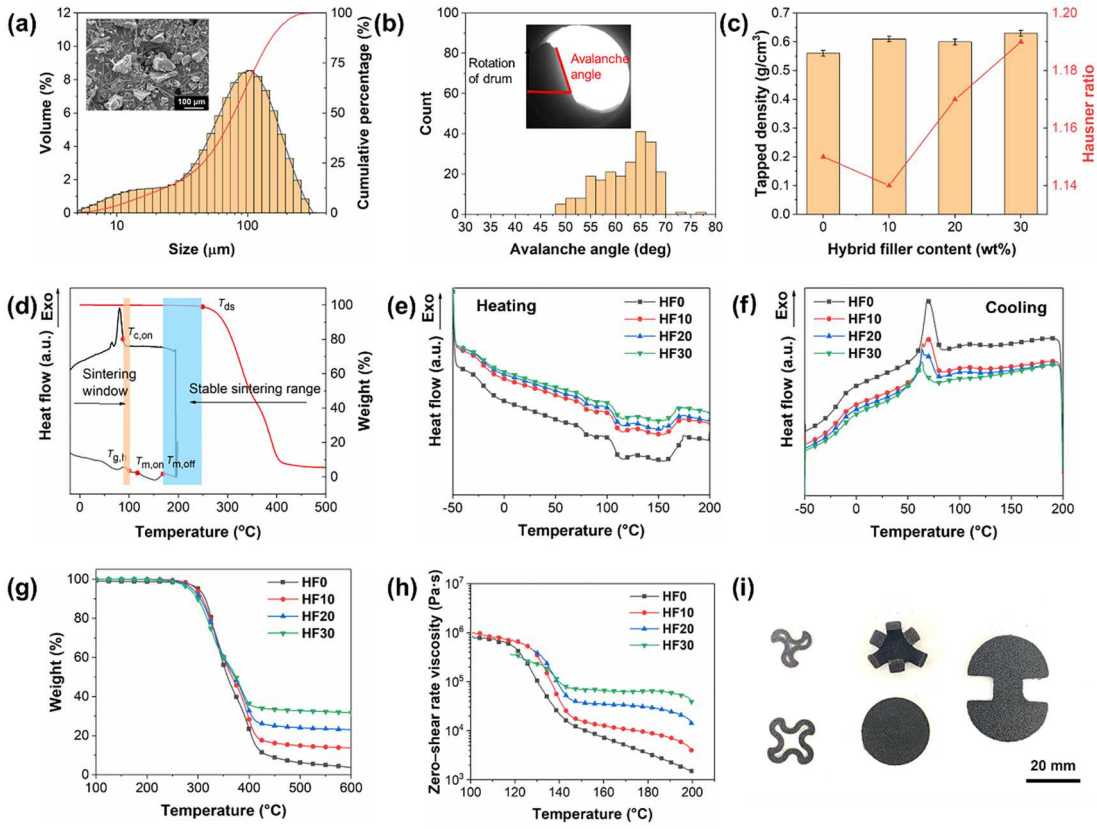

Figure 3. SLS processability evaluation of the investigated nanocomposite powders and SLS-printed parts. Powder properties including (a) the particle size distribution of the HF20 powder with the inset showing its SEM image to illustrate the powder particle morphology; (b) avalanche angles of the HF20 powder; (c) tapped density and Hausner ratio of all the investigated nanocomposite powders. Thermal properties including (d) illustration of the key thermal properties and indices of the sintering window and stable sintering range based on the neat TPU material; (e) heating behaviours of all the investigated powders; (f) cooling behaviours of all the investigated powders; (g) decomposition behaviours of all the investigated powders. Rheological properties including (h) zero–shear rate viscosity of all the investigated powders against temperature. (i) SLS-printed parts made of the prepared HF20 nanocomposite powder.

The HF10, HF20, and HF30 nanocomposite powders exhibited high median avalanche angles of 66°, 63°, and 60°, respectively (Figure 3b and Figure S2), as compared to the one of the HF0 nanocomposite powder (55°), indicating their decreased flowability. The Hausner ratio of the prepared powders increased with the increasing hybrid-filler content (Figure 3c). However, all the ratios remained below 1.25, implying the inherent free-flowing characteristic [55], which is acceptable for the SLS process. Overall, adding the rod-like hybrid filler influenced the powder properties as reflected by the increase in the surface roughness of the powder bed (Figure S3), the number of small particles, and the degraded powder flowability.

The sintering window and stable sintering range, which depend on the thermal properties of the material (Figure 3d), serve as critical indicators of the powder sinterability. A broad sintering window is preferable as it provides flexibility in setting the powder bed temperature, thereby minimising curling and warping during the printing process. A wide stable sintering range could ensure that the selected particles could achieve complete fusion without degradation.

The incorporation of the hybrid filler affected the thermal behaviours of the nanocomposite powders, consequently altering their sintering windows and stable sintering ranges. Although it had a minor influence on the glass transition temperature of the hard segments of TPU $T_{g,\,h}$ and the peak melting temperature $T_{m,\,p}$, there was a noticeable decrease in the melting enthalpy ΔH_f (Figure 3e). Additionally, the onset crystallisation temperature $T_{c,\,on}$ and crystallisation enthalpy ΔH_c (Figure 3f) were decreased, indicating an inhibition of the crystallisation process. This phenomenon has the tendency to broaden the sintering window of the prepared nanocomposite powders (Table S2), which was advantageous for the SLS process. However, the increasing hybrid-filler content led to the decreasing onset degradation temperature T_{ds} (Figure 3g). This change tended to result in a narrow stable sintering

window (Table S2), adversely affecting the SLS printing process. The reduction in T_{ds} could be mainly attributed to the degradation of HDI as the trimer of HDI was reported to start degrading at around 250 °C [50].

As the SLS process is free of shear stress, a low zero–shear rate viscosity is favoured to achieve complete particle fusion within the short sintering time. In this study, the melt viscosity of the prepared nanocomposite powders measured at 200 °C exhibited an exponential growth with the increasing hybrid-filler content (Figure 3h and Table S2) because the presence of the hybrid filler hindered the movement of the polymer chains. The high melt viscosity of the hybrid filler–reinforced nanocomposite powders could lead to their degraded coalescence behaviours and therefore poor fusion.

In summary, the addition of the hybrid filler inevitably increased the risks of the agglomeration of the powder particles at high temperatures and reduced powder flowability. As observed in Figure S3, the powder bed of the hybrid filler–reinforced nanocomposites became coarser with the increasing hybrid CF–CNT filler content. However, the warpage during the printing process could be reduced, which was reflected by the expanded sintering window. With careful process parameter determination, all the investigated nanocomposite powders were successfully employed in printing, and the SLS-printed parts made of the HF20 nanocomposite powder are shown in Figure 3i.

3.2. Mechanical and electrical properties of the nanocomposites

In this study, the optimal combination of process parameters was determined based on evaluations of the mechanical properties and microstructures of HF0 parts printed under various process parameter combinations (Figure S4). The results and discussion on optimising process parameters for the nanocomposite powders could be found in Supplementary Materials. In this study, the most suitable parameters were a scan speed of 500 mm/s and a laser power of 4.2 W, under which the nanocomposite powders with different hybrid-filler contents were fabricated.

The incorporation of the developed hybrid filler had a notable impact on the mechanical properties of the SLS-printed nanocomposites. All the nanocomposites exhibited typical elastic and plastic regions (Figure 4a). The elastic modulus was enhanced by 14.4%, 45.8%, and 8.9% for HF10, HF20, and HF30, respectively (Figure 4b and Table 1). The improvement was attributed to the high modulus of the hybrid filler. Conversely, the presence of the rigid fibres led to a pronounced reduction in the plastic region. The ultimate tensile strength decreased with the increasing hybrid-filler content. As observed from the cross-sectional images of the fractured specimens (Figure S5), the HF0 and HF10 nanocomposites exhibited relatively dense microstructures, while distinct delamination and porous microstructures were found in the HF20 and HF30 nanocomposites, leading to their reduced mechanical strength. A detailed discussion on the fracture analysis of the SLS-printed specimens can be found in the Supplementary Materials. This phenomenon also aligned with results reported in previous studies on fibre-reinforced nanocomposites [56,57].

The electrical conductivity of the SLS-printed nanocomposites varied significantly with the hybrid-filler content (Figure 4c). The neat TPU material is an electrical insulator, and its electrical conductivity was reported as 10^{-11} S/m in the literature [34,58]. The HF0 nanocomposite showed significantly enhanced electrical conductivity of 9.7×10^{-3} S/m (Table 1), which is comparable to that of materials used for the applications of sensors and electromagnetic shielding [36,59]. With an increase in the hybrid-filler content, the electrical conductivity increased by 105%, 399%, and 817%, respectively. This significant increase could be attributed to the addition of the hybrid filler, which increased the number of the electrically conductive paths and reduced the distance between the conductive paths because of the high aspect ratio of the fillers [60–62]. Additionally, the synergistic effect of CNT–OH and the fillers was conducive to improving the electrical properties of the materials.

Electrically conductive nanocomposites can be heated by applying a voltage because of the Joule heating effect [63]. The Joule heating effect transforms the electrical energy into the heat, and it is related to the electrical conductivity of the nanocomposites. In this study, the Joule heating behaviours of the developed nanocomposites were characterised under applied electric voltages of 50, 100, 150, and 200 V. After heating for 3 min, the surface temperature distribution of the nanocomposites appeared uniform. Additionally, the surface temperature increased with the increasing hybrid-filler content and applied voltage (Figure 4d). The plot of the elevated temperature ΔT by Joule heating against the heating time at a voltage of 200 V suggests that by increasing the hybrid-filler content, the time to reach the stable surface temperature decreased (Figure 4e). This reduction could be attributed to the decreased electrical resistance. It also indicates the possible enhancement in the thermal conductivity of the nanocomposites by adding the developed hybrid filler [63,64]. Considering the glass transition temperature of the nanocomposites was ~107 °C (Table S2), the voltage of 200 V was chosen to

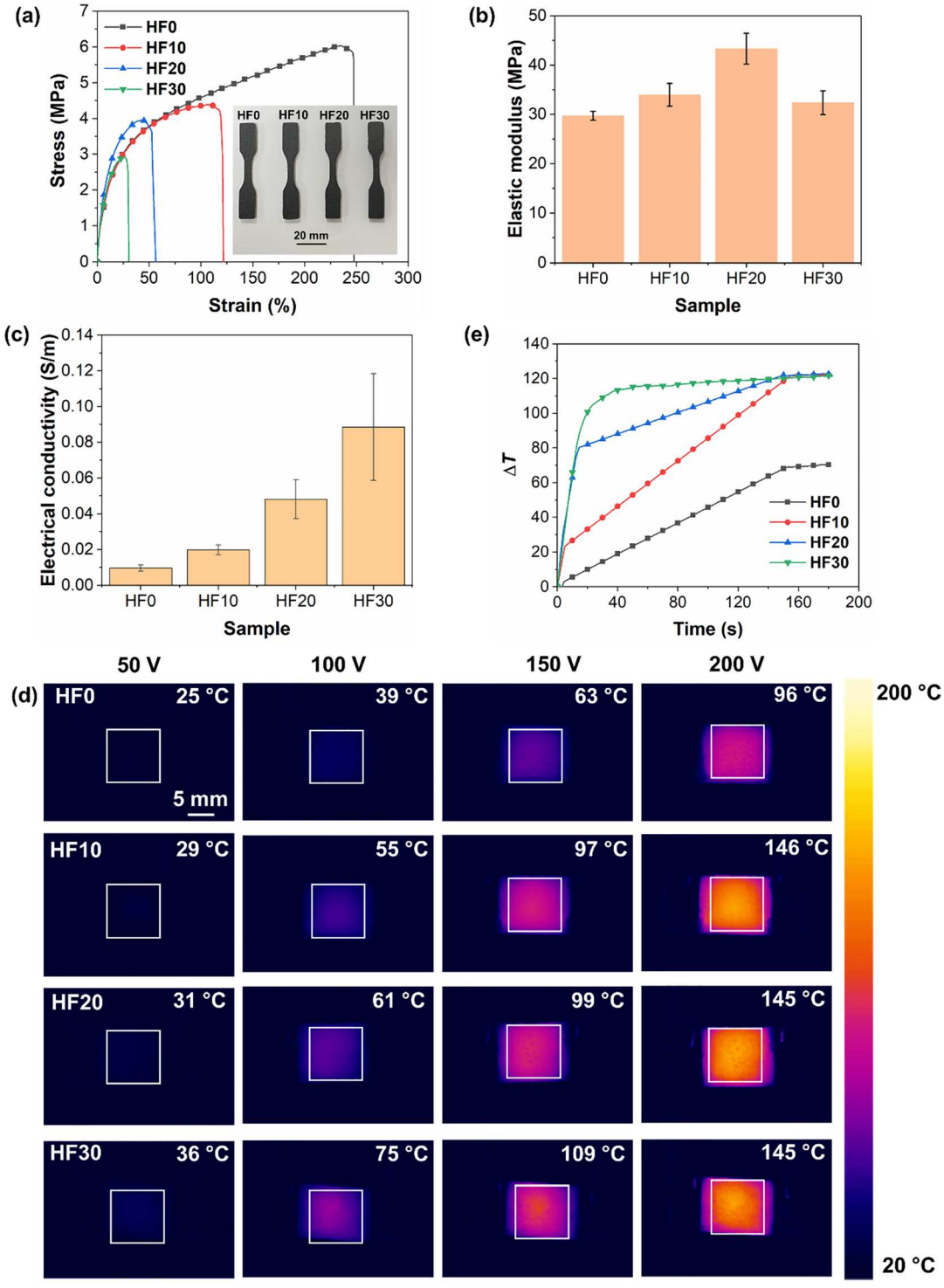

Figure 4. Mechanical and electrical properties and Joule heating behaviours of SLS-printed nanocomposites. Mechanical properties including (a) stress–strain curves; the inset is a photo of the printed specimens; (b) comparison of the elastic modulus. Electrical properties including (c) electrical conductivity. Joule heating behaviours including (d) surface temperature of the printed nanocomposites under different applied voltages after heating for 3 min; (e) plot of the elevated temperature against time at a voltage of 200 V.

trigger the shape recovery of the printed nanocomposites in the following experiments.

Overall, it could be concluded that with the addition of the hybrid filler, the mechanical and electrical properties were enhanced because of the synergistic effect between the CFs and CNTs. Additionally, an increasing hybrid-filler content led to a decrease in the ultimate tensile strength but resulted in significant

Table 1. Mechanical and electrical properties of the investigated SLS-printed nanocomposites.

Sample	Mechanical Properties			Electrical Property
	Elastic Modulus (MPa)	Ultimate Tensile Strength (MPa)	Elongation at Break (%)	Conductivity (S/m)
HF0	29.70 ± 0.91	6.10 ± 0.19	250.67 ± 18.34	$9.7 \times 10^{-3} \pm 1.8 \times 10^{-3}$
HF10	33.97 ± 2.30	4.61 ± 0.31	109.63 ± 0.54	$2.0 \times 10^{-2} \pm 2.8 \times 10^{-3}$
HF20	43.30 ± 3.14	3.94 ± 0.01	46.79 ± 3.29	$4.8 \times 10^{-2} \pm 1.1 \times 10^{-2}$
HF30	32.36 ± 2.43	2.87 ± 0.11	25.50 ± 3.46	$8.9 \times 10^{-2} \pm 3.0 \times 10^{-2}$

improvements in the electrical conductivity and temperature elevation efficiency. This trade-off between mechanical performance and improvements in other properties should be carefully evaluated when designing electro-activated shape memory nanocomposites.

3.3. Electro-activated shape memory behaviours

The shape memory behaviour of the printed nanocomposites could be divided into three consecutive steps: shape programming, shape fixation, and shape recovery (Figure 5). In this study, the nanocomposites were first programmed into temporary shapes at ~100 °C to remove the net points, which are intermolecular interactions within the materials. Subsequently, an external force was applied to alter the orientation of the macromolecular chains. The fixation of the temporary shape was achieved by cooling under stress to introduce net points into the materials to store entropy and removing the applied force. Finally, triggered by direct heating *via* a hot plate and by electricity, the temperature of the nanocomposites was elevated to remove the net points. The polymer chains recoiled to partially recover to their original shape [65]. Hence, the mechanical properties of the nanocomposites affected their shape memory properties. The HF30 nanocomposite was not used for the investigation of shape memory properties because of its relatively poor mechanical properties, which are not suitable for potential applications.

Under the condition of direct heating, all the nanocomposites started to transform into their original shapes when placed on the hot plate, and their shapes became stable after 10 min (Figure 6a). With the increasing hybrid-filler content, their R_{r_600} values decreased with values of ~40.3%, ~31%, and 18.1% (Figure 6b). Upon a voltage of 200 V, the programmed nanocomposites, exhibited accelerated shape recovery behaviours under electric currents compared to those triggered by the hot plate (Figure 6c), suggesting the higher efficiency of the electro-activated shape recovery. This phenomenon could be explained by the formation of an electrically conductive network, which led to the more homogenous thermal distribution driven by the Joule heating effect within the printed nanocomposites. In contrast, direct heating depends more on the thermal conduction from the hot plate. Additionally, it was found that the shape recovery speed increased when increasing the hybrid-filler content, which could be attributed to the enhanced conductivity (Figure 4c) and the resulting high temperature elevation efficiency (Figure 4e). In practical terms, fast response means that the nanocomposites could be used in applications requiring quick, reliable shape changes, such as in sensors or actuators where rapid response is critical. Remarkably, the HF20 nanocomposite exhibited the highest R_{r_25} value, suggesting it recovered fastest in the duration of 25 s (Figure 6d). This shape recovery speed was comparable to that of other reported nanocomposites with a high carbon-black content of 25 wt% [66], suggesting that the HF20 nanocomposites achieved higher efficiency with a lower filler content. The fast response of the HF20 nanocomposite to electricity makes it promising for the application of remotely controlled smart components. Similarly, the R_{r_600} values of the developed nanocomposites upon the electricity trigger were found to decrease with the increasing hybrid-filler content.

The incomplete shape recovery of the printed nanocomposites in this study could be ascribed to the hindering effect of the fillers on the movement of the polymer chains. Figures 3f and 4a illustrate that the crystallisation enthalpy and elongation at break decreased with the increasing hybrid-filler content, suggesting the gradually decreased polymer chain flexibility. Additionally, two more factors could influence the shape recovery process as well. The first is the friction between the polymer chains and the introduced fillers [67]. The second is the insufficient elevated temperature, affected by both the microstructure and the environment temperature [68], which needs to be sufficiently high to fully remove the net points within the materials. In the future, to enhance the electro-activated shape memory performance, it would be beneficial to improve the interaction between the developed hybrid filler and the CNT–OH–coated TPU particles to optimise the microstructure of the SLS-printed nanocomposites. Additionally, optimising the chemical structure of TPU could lead to improved shape memory properties and better processability in SLS.

Smart components with specific stimulus-dependent configuration over time are promising for various

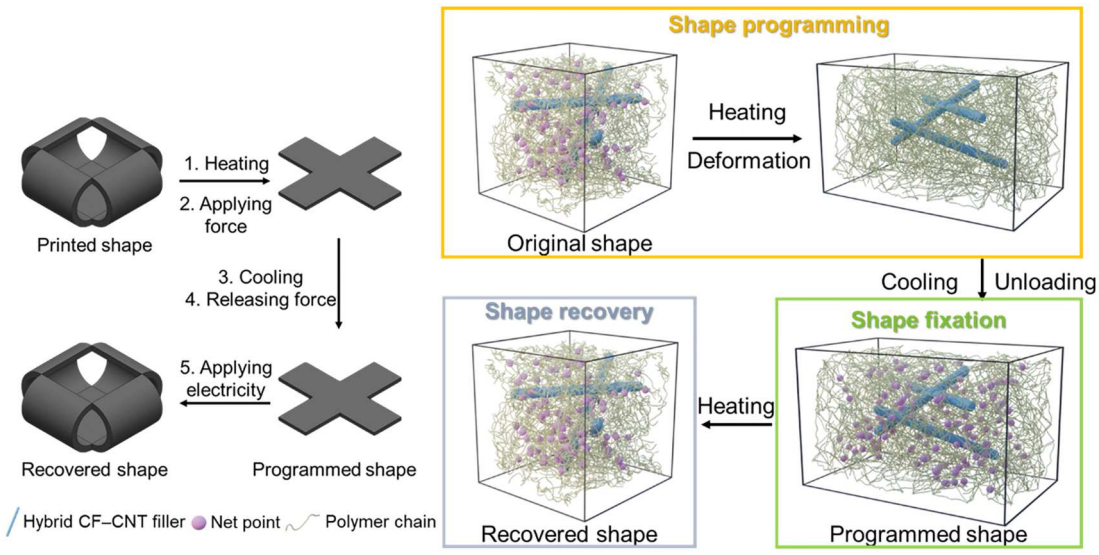

Figure 5. Electro-activated shape memory behaviours of SLS-printed nanocomposite and its underlying mechanism.

applications in prototyping, aerospace engineering, biomedical engineering [26,69], *etc*. In this study, a smart component made of the HF20 nanocomposite was fabricated to demonstrate its potential to achieve specific functionality by changing its shape through the site-specific control *via* electric currents. The printed structure was first programmed to bend and achieve the locking functionality (Figure 7a). Then, two sites of the bent structures were individually connected to a source metre through a manual control (Figure 7b). When only Site I was subjected to electric currents, only the shape of Site I started to recover, while the

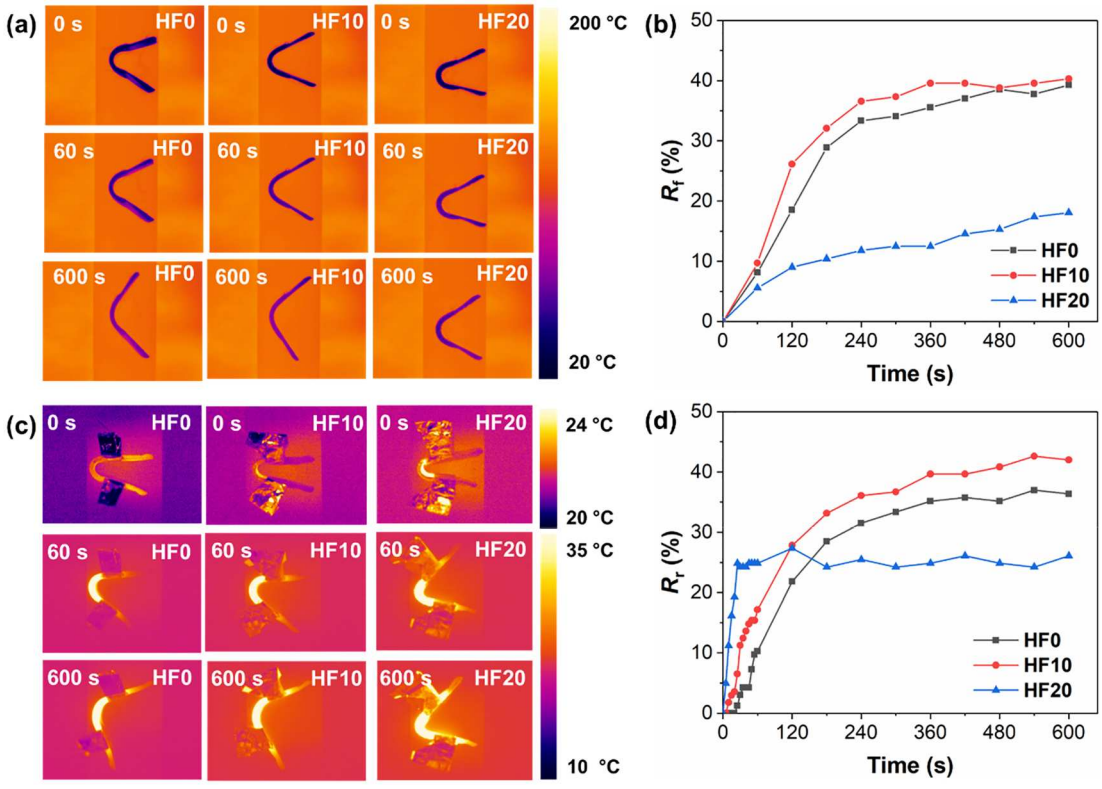

Figure 6. Shape memory behaviours of SLS-printed nanocomposites: (a) shape recovery process and (b) shape recovery ratio at different time for the direct-heating triggering method with a hot plate of 120 °C; (c) shape recovery process and (d) shape recovery ratio at different time for the electricity triggering method.

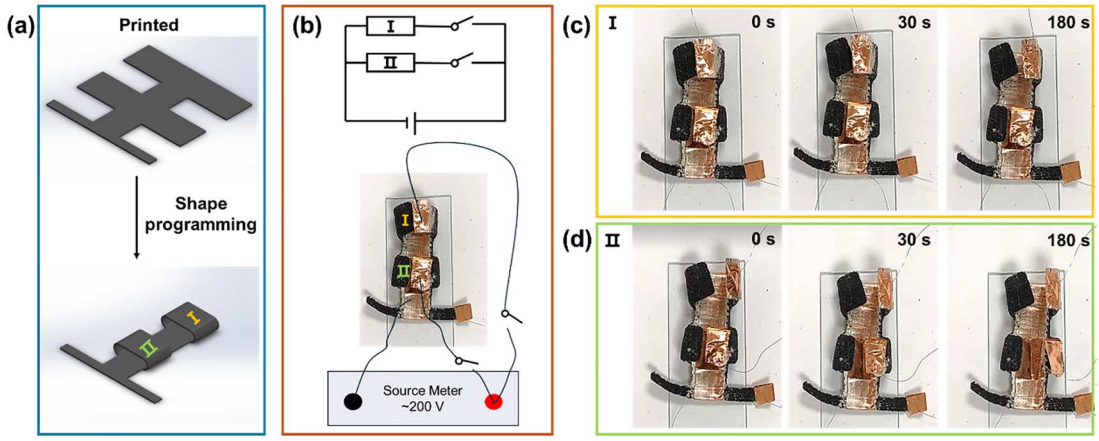

Figure 7. Demonstration of a printed nanocomposite for potential applications in remotely and selectively controlled smart components: (a) design of the printed structure and the shape-programmed structure; (b) circuit design and experiment settings to trigger the electro-activated shape memory behaviours of the printed structure; (c and d) shape recovery process of Site I and Site II of the programmed structures.

shape of Site II remained unchanged without electrical currents. After a few minutes, the structure at Site I opened, demonstrating the releasing functionality (Figure 7c). Subsequently, Site II was connected to the source metre, causing its shape to recover (Figure 7d). These smart components enable remote and selective control to achieve locking and releasing functions. With a proper structural design, the developed nanocomposites are also promising for applications such as actuators for soft robotics, expandable structures for aerospace engineering, and sequential folding structures.

4. Conclusions

This work is the first study to fabricate electro-activated shape memory materials *via* SLS 3D printing. A novel multiscale hybrid filler was developed by grafting hydroxylated CNTs on the surface of plasma-treated CFs with the assistance of HDI. The multiscale hybrid filler was then mixed with CNT-coated TPU powders to prepare multi-functional nanocomposite powders. The addition of the hybrid filler was found to enhance the electrical and thermal properties because of the increase in the number of conductive paths and the decrease in the spacing between the conductive paths. The shape recovery of the HF20 nanocomposite was almost four times faster when triggered by electric currents than that triggered by the direct-heating method and exhibited a higher shape recovery ratio. The electro-activated method exhibited advantages in the homogenous thermal distribution and fast shape recovery speed, enabling its potential applications in fabricating remotely controlled smart components. A remotely and selectively controlled smart component was designed and fabricated to demonstrate the potential applications of the developed materials in this work.

Although this study proposes novel electro-activated shape memory TPU nanocomposites fabricated using the SLS technique, several limitations need to be addressed in future work. First, the electro-activated shape recovery ratio and efficiency could be further enhanced through polymer matrix modification to meet real-world application demands. Additionally, it is crucial to establish quantitative relationships between the shape recovery performance and applied current, which would provide a comprehensive understanding and facilitate the optimisation of these materials for practical use.

Acknowledgements

The authors would like to acknowledge the support from the Singapore Institute of Manufacturing Technology (SIMTech)–NTU 3D Additive Manufacturing Joint Laboratory. and Singapore Centre for 3D Printing (SC3DP).

Disclosure statement

No potential conflict of interest was reported by the author(s).

Data availability statement

The data that support the findings of this study are available from the corresponding author upon reasonable request.

ORCID

Yujia Tian http://orcid.org/0000-0002-6032-4715
Kun Zhou http://orcid.org/0000-0001-7660-2911

References

[1] Rahmatabadi D, Soleyman E, Fallah Min Bashi M, et al. 4D printing and annealing of PETG composites reinforced with short carbon fibers. Phys Scr. 2024;99:055957. doi:10.1088/1402-4896/ad3b40

[2] Rahmatabadi D, Khajepour M, Bayati A, et al. Advancing sustainable shape memory polymers through 4D printing of polylactic acid-polybutylene adipate terephthalate blends. Eur Polym J. 2024;216:113289, doi:10.1016/j.eurpolymj.2024.113289

[3] Aberoumand M, Rahmatabadi D, Soltanmohammadi K, et al. Stress recovery and stress relaxation behaviors of PVC 4D printed by FDM technology for high-performance actuation applications. Sensors Actuators A Phys. 2023;361:114572, doi:10.1016/j.sna.2023.114572

[4] Leng J, Lan X, Liu Y, et al. Shape-memory polymers and their composites: stimulus methods and applications. Prog Mater Sci. 2011;56:1077–1135. doi:10.1016/j.pmatsci.2011.03.001

[5] van Manen T, Janbaz S, Jansen KMB, et al. 4D printing of reconfigurable metamaterials and devices. Commun Mater. 2021;2:56. doi:10.1038/s43246-021-00165-8

[6] Li A, Challapalli A, Li G. 4D printing of recyclable lightweight architectures using high recovery stress shape memory polymer. Sci Rep. 2019;9:7621. doi:10.1038/s41598-019-44110-9

[7] Dong K, Panahi-Sarmad M, Cui Z, et al. Electro-induced shape memory effect of 4D printed auxetic composite using PLA/TPU/CNT filament embedded synergistically with continuous carbon fiber: a theoretical & experimental analysis. Compos Part B Eng. 2021;220:108994, doi:10.1016/j.compositesb.2021.108994

[8] Yang C, Boorugu M, Dopp A, et al. 4D printing reconfigurable, deployable and mechanically tunable metamaterials. Mater Horizons. 2019;6:1244–1250. doi:10.1039/c9mh00302a

[9] Mohol SS, Sharma V. Functional applications of 4D printing: a review. Rapid Prototyp J. 2021;27:1501–1522. doi:10.1108/RPJ-10-2020-0240

[10] Bodaghi M, Liao WH. 4D printed tunable mechanical metamaterials with shape memory operations. Smart Mater Struct. 2019;28:045019. doi:10.1088/1361-665X/ab0b6b

[11] Huang X, Panahi-Sarmad M, Dong K, et al. Tracing evolutions in electro-activated shape memory polymer composites with 4D printing strategies: a systematic review. Compos Part A Appl Sci Manuf. 2021;147:106444. doi:10.1016/j.compositesa.2021.106444

[12] Wang K, Lin F, Lai DTH, et al. Soft gold nanowire sponge antenna for battery-free wireless pressure sensors. Nanoscale. 2021;13:3957–3966. doi:10.1039/D0NR07621J

[13] Yap LW, Gong S, Tang Y, et al. Soft piezoresistive pressure sensing matrix from copper nanowires composite aerogel. Sci Bull. 2016;61:1624–1630. doi:10.1007/s11434-016-1149-0

[14] Kim J-Y, Jang K-S. Facile fabrication of stretchable electrodes by sedimentation of Ag nanoparticles in PDMS matrix. J Nanomater. 2018;2018:1–6. doi:10.1155/2018/4580921

[15] Sun H, Yang Z, Pu Y, et al. Zinc oxide/vanadium pentoxide heterostructures with enhanced day-night antibacterial activities. J Colloid Interface Sci. 2019;547:40–49. doi:10.1016/j.jcis.2019.03.061

[16] Iranagh SA, Eskandarian L, Mohammadi R. Synthesis of MnO2-polyaniline nanofiber composites to produce high conductive polymer. Synth Met. 2013;172:49–53. doi:10.1016/j.synthmet.2013.04.002

[17] Wu S, Zhang J, Ladani RB, et al. Novel electrically conductive porous PDMS/carbon nanofiber composites for deformable strain sensors and conductors. ACS Appl Mater Interfaces. 2017;9:14207–14215. doi:10.1021/acsami.7b00847

[18] Wu S, Peng S, Han ZJ, et al. Ultrasensitive and stretchable strain sensors based on mazelike vertical graphene network. ACS Appl Mater Interfaces. 2018;10:36312–36322. doi:10.1021/acsami.8b15848

[19] Nadgorny M, Ameli A. Functional polymers and nanocomposites for 3D printing of smart structures and devices. ACS Appl Mater Interfaces. 2018;10:17489–17507. doi:10.1021/acsami.8b01786

[20] Wang X, Jiang M, Zhou Z, et al. 3D printing of polymer matrix composites: a review and prospective. Compos Part B Eng. 2017;110:442–458. doi:10.1016/j.compositesb.2016.11.034

[21] Gackowski BM, Goh GD, Sharma M, et al. Additive manufacturing of nylon composites with embedded multimaterial piezoresistive strain sensors for structural health monitoring. Compos. Part B Eng. 2023;261:110796. doi:10.1016/j.compositesb.2023.110796

[22] Leigh SJ, Bradley RJ, Purssell CP, et al. A simple, low-cost conductive composite material for 3D printing of electronic sensors. PLoS One. 2012;7:e49365. doi:10.1371/journal.pone.0049365

[23] Kokkinis D, Schaffner M, Studart AR. Multimaterial magnetically assisted 3D printing of composite materials. Nat Commun. 2015;6:8643. doi:10.1038/ncomms9643

[24] Lee SL, Chang C-J. Recent developments about conductive polymer based composite photocatalysts. Polymers (Basel). 2019;11:206. doi:10.3390/polym11020206

[25] Chen J, Zhu Y, Huang J, et al. Advances in responsively conductive polymer composites and sensing applications. Polym Rev. 2021;61:157–193. doi:10.1080/15583724.2020.1734818

[26] Kuang X, Roach DJ, Wu J, et al. Advances in 4D printing: materials and applications. Adv Funct Mater. 2019;29:1805290. doi:10.1002/adfm.201805290

[27] Fu P, Li H, Gong J, et al. 4D printing of polymers: techniques, materials, and prospects. Prog Polym Sci. 2021;126:101506.

[28] Zhang Z, Demir KG, Gu GX. Developments in 4D-printing: a review on current smart materials, technologies, and applications. Int J Smart Nano Mater. 2019;10:205–224. doi:10.1080/19475411.2019.1591541

[29] Shao LH, Zhao B, Zhang Q, et al. 4D printing composite with electrically controlled local deformation. Extrem Mech Lett. 2020;39:100793, doi:10.1016/j.eml.2020.100793

[30] Zeng C, Liu L, Bian W, et al. 4D printed electro-induced continuous carbon fiber reinforced shape memory polymer composites with excellent bending resistance. Compos Part B Eng. 2020;194:108034. doi:10.1016/j.compositesb.2020.108034

[31] Dong X, Zhang F, Wang L, et al. 4D printing of electroactive shape-changing composite structures and their programmable behaviors. Compos Part A Appl Sci Manuf. 2022;157:106925. doi:10.1016/j.compositesa.2022.106925

[32] Zhou Y, Yang Y, Jian A, et al. Co-extrusion 4D printing of shape memory polymers with continuous metallic fibers for selective deformation. Compos Sci Technol. 2022;227:109603. doi:10.1016/j.compscitech.2022.109603

[33] Cortés A, Cosola A, Sangermano M, et al. DLP 4D-printing of remotely, modularly, and selectively controllable shape memory polymer nanocomposites embedding carbon nanotubes. Adv Funct Mater. 2021;31:2106774. doi:10.1002/adfm.202106774

[34] Li Z, Wang Z, Gan X, et al. Selective laser sintering 3D printing: a way to construct 3D electrically conductive segregated network in polymer matrix. Macromol Mater Eng. 2017;302:1700211. doi:10.1002/mame.201700211

[35] Xiang D, Zhang X, Li Y, et al. Enhanced performance of 3D printed highly elastic strain sensors of carbon nanotube/thermoplastic polyurethane nanocomposites via non-covalent interactions. Compos Part B Eng. 2019;176:107250. doi:10.1016/j.compositesb.2019.107250

[36] Yuan S, Zheng Y, Chua CK, et al. Electrical and thermal conductivities of MWCNT/polymer composites fabricated by selective laser sintering. Compos Part A Appl Sci Manuf. 2018;105:203–213. doi:10.1016/j.compositesa.2017.11.007

[37] Yuan S, Shen F, Bai J, et al. 3D soft auxetic lattice structures fabricated by selective laser sintering: TPU powder evaluation and process optimization. Mater Des. 2017;120:317–327. doi:10.1016/j.matdes.2017.01.098

[38] Qi F, Chen N, Wang Q. Dielectric and piezoelectric properties in selective laser sintered polyamide11/BaTiO3/CNT ternary nanocomposites. Mater Des. 2018;143:72–80. doi:10.1016/j.matdes.2018.01.050

[39] Zhou M, Zhu W, Yu S, et al. Selective laser sintering of carbon nanotube–coated thermoplastic polyurethane: mechanical, electrical, and piezoresistive properties. Compos Part C Open Access. 2022;7:100212. doi:10.1016/j.jcomc.2021.100212

[40] Mei S, Zhang X, Ding B, et al. 3D-Printed thermoplastic polyurethane/graphene composite with porous segregated structure: toward ultralow percolation threshold and great strain sensitivity. J Appl Polym Sci. 2021;138:50168. doi:10.1002/app.50168

[41] Gan X, Wang J, Wang Z, et al. Simultaneous realization of conductive segregation network microstructure and minimal surface porous macrostructure by SLS 3D printing. Mater Des. 2019;178:107874. doi:10.1016/j.matdes.2019.107874

[42] Ronca A, Rollo G, Cerruti P, et al. Selective laser sintering fabricated thermoplastic polyurethane/graphene cellular structures with tailorable properties and high strain sensitivity. Appl Sci. 2019;9:1–15. doi:10.3390/app9050864

[43] Zhuang Y, Guo Y, Li J, et al. Preparation and laser sintering of a thermoplastic polyurethane carbon nanotube composite-based pressure sensor. RSC Adv. 2020;10:23644–23652. doi:10.1039/d0ra04479b

[44] Zhuang Y, Guo Y, Li J, et al. Study on the forming and sensing properties of laser-sintered TPU/CNT composites for plantar pressure sensors. Int J Adv Manuf Technol. 2021;112:2211–2222. doi:10.1007/s00170-020-06560-8

[45] Zhou M, Zhu W, Yu S, et al. Comparative study on selective laser sintering of aromatic and aliphatic thermoplastic polyurethanes: processability, microstructure, and mechanical properties. J Micromechanics Mol Phys. 2022;8:11–24. doi:10.1142/S2424913022500023

[46] Zheng H, Zhang W, Li B, et al. Recent advances of interphases in carbon fiber-reinforced polymer composites: a review. Compos Part B Eng. 2022;233:109639. doi:10.1016/j.compositesb.2022.109639

[47] Wang H, Duan Y, Ma X, et al. Polyisocyanate bridged environmental graphene/epoxy nanocomposite coatings with excellent anticorrosion performance. Prog Org Coatings. 2021;153:106167. doi:10.1016/j.porgcoat.2021.106167

[48] Radjef R, Jarvis KL, Fox BL, et al. Comparing the properties of commercially treated and air plasma treated carbon fibers. Surf Coatings Technol. 2021;408:126751. doi:10.1016/j.surfcoat.2020.126751

[49] Han J, Yeom J, Mensing G, et al. Surface energy approach and AFM verification of the (CF)n treated surface effect and its correlation with adhesion reduction in microvalves. J Micromech Microeng. 2009;19:085017. doi:10.1088/0960-1317/19/8/085017

[50] Li X, Wang H, Zhang Z, et al. Effect of covalent functionalization of multi-walled carbon nanotubes with HDI trimer on mechanical properties of polyaspartate polyurea. Mater Res Express. 2021;8:1–12. doi:10.1088/2053-1591/ac1768

[51] Han SH, Oh HJ, Kim SS. Evaluation of fiber surface treatment on the interfacial behavior of carbon fiber-reinforced polypropylene composites. Compos Part B Eng. 2014;60:98–105. doi:10.1016/j.compositesb.2013.12.069

[52] Kleijnen R, Schmid M, Wegener K. Production and processing of a spherical polybutylene terephthalate powder for laser sintering. Appl Sci. 2019;9:1308. doi:10.3390/app9071308

[53] Ziegelmeier S, Christou P, Wöllecke F, et al. An experimental study into the effects of bulk and flow behaviour of laser sintering polymer powders on resulting part properties. J Mater Process Technol. 2015;215:239–250. doi:10.1016/j.jmatprotec.2014.07.029

[54] Goodridge RD, Tuck CJ, Hague RJM. Laser sintering of polyamides and other polymers. Prog Mater Sci. 2012;57:229–267. doi:10.1016/j.pmatsci.2011.04.001

[55] Tan LJ, Zhu W, Sagar K, et al. Comparative study on the selective laser sintering of polypropylene homopolymer and copolymer: processability, crystallization kinetics, crystal phases and mechanical properties. Addit Manuf. 2021;37:101610, doi:10.1016/j.addma.2020.101610

[56] Chen J, Tan P, Liu X, et al. High-strength light-weight aramid fibre/polyamide 12 composites printed by multi Jet fusion. Virtual Phys Prototyp. 2022;17:295–307. doi:10.1080/17452759.2022.2036931

[57] Chen J, Zhao L, Zhou K. Improvement in the mechanical performance of multi jet fusion–printed aramid fiber/polyamide 12 composites by fiber surface modification.

Addit Manuf. 2022;51:102576. doi:10.1016/j.addma.2021.102576

[58] Liu H, Li Y, Dai K, et al. Electrically conductive thermoplastic elastomer nanocomposites at ultralow graphene loading levels for strain sensor applications. J Mater Chem C. 2015;4:157–166. doi:10.1039/c5tc02751a

[59] Rollo G, Ronca A, Cerruti P, et al. Optimization of piezoresistive response of elastomeric porous structures based on carbon-based hybrid fillers created by selective laser sintering. Polymers (Basel). 2023;15:4404. doi:10.3390/polym15224404

[60] Sang Z, Ke K, Manas-Zloczower I. Effect of carbon nanotube morphology on properties in thermoplastic elastomer composites for strain sensors. Compos Part A Appl Sci Manuf. 2019;121:207–212. doi:10.1016/j.compositesa.2019.03.007

[61] Alig I, Pötschke P, Lellinger D, et al. Establishment, morphology and properties of carbon nanotube networks in polymer melts. Polymer (Guildf). 2012;53:4–28. doi:10.1016/j.polymer.2011.10.063

[62] Bauhofer W, Kovacs JZ. A review and analysis of electrical percolation in carbon nanotube polymer composites. Compos Sci Technol. 2009;69:1486–1498. doi:10.1016/j.compscitech.2008.06.018

[63] Meng H, Li G. A review of stimuli-responsive shape memory polymer composites. Polymer (Guildf). 2013;54:2199–2221. doi:10.1016/j.polymer.2013.02.023

[64] Yuan S, Bai J, Chua CK, et al. Highly enhanced thermal conductivity of thermoplastic nanocomposites with a low mass fraction of MWCNTs by a facilitated latex approach. Compos Part A Appl Sci Manuf. 2016;90:699–710. doi:10.1016/j.compositesa.2016.09.002

[65] Lendlein A, Gould OEC. Reprogrammable recovery and actuation behaviour of shape-memory polymers. Nat Rev Mater. 2019;4:116–133. doi:10.1038/s41578-018-0078-8

[66] Arun DI, Kumar KSS, Kumar BS, et al. High glass-transition polyurethane-carbon black electro-active shape memory nanocomposite for aerospace systems. Mater Sci Technol. 2019;35:596–605. doi:10.1080/02670836.2019.1575054

[67] Abrisham M, Panahi-Sarmad M, Sadeghi GMM, et al. Microstructural design for enhanced mechanical property and shape memory behavior of polyurethane nanocomposites: role of carbon nanotube, montmorillonite, and their hybrid fillers. Polym Test. 2020;89:106642. doi:10.1016/j.polymertesting.2020.106642

[68] Shao LH, Zhao B, Zhang Q, et al. 4D printing composite with electrically controlled local deformation. Extrem Mech Lett. 2020;39:100793. doi:10.1016/j.eml.2020.100793

[69] Kim H, Kim K-H, Jeong J, et al. Recent progress on materials for functional additive manufacturing. Mater Sci Addit Manuf. 2024;3:3323. doi:10.36922/msam.3323.